A&A 390, 1–12 (2002)
DOI: 10.1051/0004-6361:20020720

Astronomy & Astrophysics

Cosmology with galaxy clusters in the XMM large-scale structure survey

A. Refregier[1], I. Valtchanov[2], and M. Pierre[2]

[1] Institute of Astronomy, Madingley Road, Cambridge CB3 OHA, UK
e-mail: `ar@ast.cam.ac.uk`
[2] Service d'Astrophysique, Bât. 709, CEA Saclay, 91191 Gif-sur-Yvette, France
e-mail: `ivaltchanov;mpierre@cea.fr`

Received 28 September 2001 / Accepted 13 May 2002

Abstract. The upcoming XMM Large Scale Structure Survey (XMM-LSS) will ultimately provide a unique mapping of the distribution of X-ray sources in a contiguous 64 deg^2 region. In particular, it will provide the 3-dimensional location of about 900 galaxy clusters out to a redshift of about 1. We study the prospects that this cluster catalogue offers for measuring cosmological parameters. We use the Press-Schechter formalism to predict the counts of clusters and their X-ray properties in several CDM models. We compute the detection efficiency of clusters, using realistic simulations of XMM X-ray images, and study how it differs from a conventional flux limit. We compute the expected correlation function of clusters using the extended halo model, and show that it is expected to evolve very little out to $z \simeq 2$, once the selection function of the survey is taken into account. The shape and the amplitude of the correlation function can be used to brake degeneracies present when cluster counts alone are considered. Ignoring systematic uncertainties, the combination of cluster counts evolution and of the correlation function yields measurements of $\Omega_{\rm m}$, σ_8 and Γ with a precision of about 15%, 10% and 35%, respectively, in a ΛCDM model. This combination will also provide a consistency check for the ΛCDM model, and a discrimination between this model and the OCDM model. The XMM-LSS will therefore provide important constraints on cosmological parameters, complementing that from other methods such as the Cosmic Microwave Background. We discuss how these constraints are affected by instrumental systematics and by the uncertainties in the scaling relations of clusters.

Key words. X-rays: galaxies: clusters – galaxies: clusters: general – cosmology: cosmological parameters – cosmology: large-scale structure of Universe – surveys

1. Introduction

Clusters of galaxies are the most massive bound objects in the Universe and provide a powerful cosmological probe (see e.g. Borgani & Guzzo 2001 for a review). In particular, the number counts of clusters and its evolution yield a robust measure of both the amplitude of the matter power spectrum and of the geometry of the universe (e.g. Oukbir & Blanchard 1997; Eke et al. 1998; Viana & Liddle 1999; Kitiyama & Suto 1997). The spatial correlation function of clusters quantifies the clustering of these objects and yields complementary constraints on cosmology (e.g. Mo et al. 1996; Suto et al. 2000; Robinson 2000; Moscardini et al. 2000; Collins et al. 2000).

In this paper, we explore the prospects of measuring cosmological parameters with the upcoming XMM Large Scale Structure Survey (XMM-LSS; Pierre 2000). This survey consists of 10 ksec exposures of an 8 × 8 deg^2 region with the XMM-Newton observatory, along with an extensive follow-up programme in the optical, IR and radio bands. In particular, it will provide the 3-dimensional location of about 900 clusters out to a redshift of about 1. Thanks to its uniform sensitivity across a contiguous region, this survey thus provides a unique database to measure the evolution of both the number counts and the correlation function of clusters.

To study how the clusters found in XMM-LSS can constrain cosmological models, we use the Press & Schechter (1974) formalism to predict the expected cluster counts in the survey. This is done using the selection function of the survey derived from detailed simulations of cluster detections in XMM-Newton images (see Valtchanov et al. 2001, VPG). Using the Mo & White (1996) formalism, we compute the expected spatial correlation function for the detected clusters. We then study how the cluster counts and correlation function, taken together, constrain cosmological parameters.

Our analysis extends the work of Moscardini et al. (2000) who considered the expected cluster counts and correlation function for XMM-LSS. They however assumed a simple flux limit, rather than the more realistic selection function which we consider. In addition, they did not compute the cosmological constraints from a joint measurement of the cluster counts

---

Send offprint requests to: A. Refregier,
e-mail: `ar@ast.cam.ac.uk`

and correlation function with XMM-LSS. Our results also complement the analysis of Romer et al. (2001) who studied the cosmological dependence of cluster counts in the planned Serendipitous XMM Cluster Survey. They are also related to the work of Haiman al. (2001) and Holder et al. (2001) who studied the cosmological constraints which can be derived from the evolution of cluster counts with a dedicated wide-angle X-ray mission.

The paper is organized as follows. In Sect. 2 we summarize the characteristics of the XMM-LSS. In Sect. 3, we describe the simulations for cluster detection and derive the cluster selection function. In Sect. 4 we compute the expected cluster counts using the selection function combined with the Press-Schechter formalism. In Sect. 5 we compute the correlation function for this cluster sample and show how it constrains cosmological parameters. The effects of systematic uncertainties on these constraints are discussed in Sect. 6. Our conclusions are summarized in Sect. 7.

2. The XMM large scale structure survey

The XMM-LSS Survey is a unique medium-deep cluster survey combining X-ray observations with an extensive optical, IR, and radio follow-up programme (Pierre 2000). The survey geometry – coverage and depth – was chosen to allow the measurement of the cluster two-point correlation function, with better than 15% error on the correlation length, in two redshift intervals between $z = 0$ and 1.

The position of the 8×8 deg^2 surveyed area on the sky ($\alpha = 2^{\rm h}20^{\rm m}$, $\delta = -5^{\rm o}$) is at a sufficiently high galactic latitude ($\approx -60^{\rm o}$) in a region of moderate galactic absorption and without known bright X-ray sources. It will be covered by 24×24 partially overlapping XMM pointings with individual exposure times of 10 ks, reaching a sensitivity of 3×10^{-15} erg s^{-1} cm^{-2} in the [0.5–2] keV band for point sources, or of about 5×10^{-15} erg s^{-1} cm^{-2} for cluster-like extended sources. Down to this limit, some 300 objects (mainly QSOs) per deg^2 are expected according to the latest deep surveys (e.g. Hasinger et al. 2001; Giacconi et al. 2001), and a total of about 10–15 clusters per deg^2 out to $z \simeq 1$. The survey is also well suited to probe the existence of massive clusters within the important $1 < z < 2$ redshift range. At the time of writing, 6 deg^2 with XMM have been allocated in guaranteed time and guest observer time. The rest of the survey is subject to an ongoing application and reviewing process.

An extensive multi-wavelength follow-up programme has been undertaken by the XMM-LSS consortium[1]. Special care is given to the optical identification of the X-ray sources: deep multi-color imaging of the entire region will be performed by the Canada-France-Hawaii Legacy Survey[2] and subsequent redshift measurements by the VIRMOS/VLT instrument and other large telescopes to which the consortium has access. The main priorities are: (1) identification and redshift measurement of all X-ray clusters between $0 < z < 1$, (2) NIR observations of distant ($z > 1$) cluster candidates and, subsequently, determination of their redshift, (3) serendipitous spectroscopic observations of the X-ray QSOs, in order to study their clustering properties within the deep potential-well network traced by the clusters.

3. Simulations

In order to estimate the detection probability of clusters in the survey, we performed a series of X-ray image simulations. While a detailed description can be found in VPG, we first review here the main features of the simulations. We then show how they can be used to derive the selection function for the survey.

3.1. Cluster detection in simulated images

The simulations reproduce the main characteristics of the XMM-EPIC instruments, such as the Point-Spread Function (assuming circular symmetry for the PSF shape; see VPG) and vignetting as a function of energy and off-axis angle. These were parametrized using the latest available on-flight calibrations. For the diffuse and particle background, we have used the data from Watson et al. (2001).

The point-like sources were laid at random inside the field-of-view. Their fluxes were drawn from the $\log N - \log S$ data in Lockman Hole (Hasinger et al. 2001) and Chandra deep field south (Giacconi et al. 2001). Their spectrum was taken to be a power law with photon index 2.

Clusters of galaxies were modeled as spherically symmetric objects assuming a β-profile (e.g. Cavaliere & Fusco-Femiano 1976) with fixed core radius $r_{\rm c} = 125\ h^{-1}$ kpc and slope $\beta = 0.75$ (see Sect. 6 for a discussion of the effect of a varying core radius on our predictions). A thermal plasma spectrum (Raymond & Smith 1977) was assumed. The spectrum was normalized using the non-evolving luminosity-temperature ($L-T$) relation of Arnaud & Evrard (1999). When generalized to arbitrary cosmological model, it is given by

$$L = 2.87 \times 10^{44} \left(\frac{T}{6\ \rm keV}\right)^{2.88} \left(\frac{D_L}{D_{L,\rm EdS}}\right)^2 h^{-2}\ {\rm erg\ s^{-1}}, \qquad (1)$$

where L is the bolometric luminosity, T is the X-ray temperature, and D_L and $D_{L,\rm EdS}$ are the luminosity distances in the desired and Einstein-de Sitter cosmological models, respectively.

We took the neutral hydrogen column density to be $N_H = 5 \times 10^{20}$ cm^{-2} and element abundances $Z = 0.3\ Z_\odot$. Using XSPEC (Arnaud 1996), we calculated the total expected count rates for the extended and point-like sources for the three XMM EPIC instruments[3] with thin filters in [0.5–2] keV energy band, for an integration time of 10 ks.

For a given temperature and redshift, we placed 13 clusters with centers on a grid inside the inner 10′ radius of the field-of-view. This number was chosen to maximally fill this region while avoiding overlaps. The grid pattern can be seen in the

---

[1] Official web page of the consortium:
`http://vela.astro.ulg.ac.be/themes/spatial/xmm/LSS/`

[2] `http://cdsweb.u-strasbg.fr:2001/Instruments/Imaging/ Megacam`

[3] See e.g. the XMM-Newton User's Handbook:
`http://xmm.vilspa.esa.es/user/uhb/xmm_uhb.html`

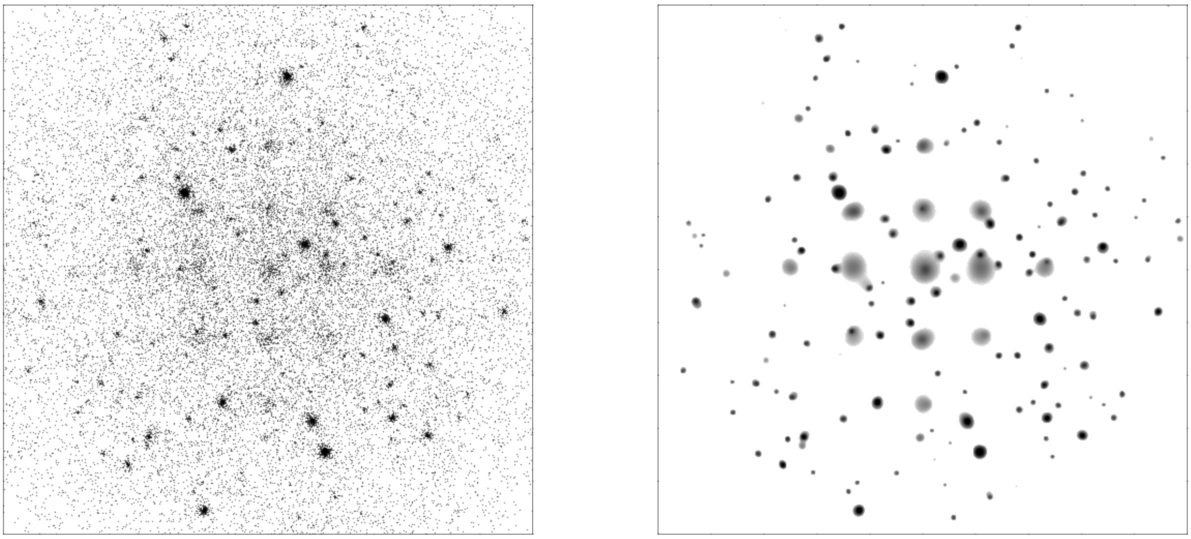

Fig. 1. Simulated extragalactic XMM-LSS raw image (left) and the corresponding wavelet filtered image with Poisson noise model and 10^{-4} ($\sim 4\sigma$) significance (Starck & Pierre 1998). The energy band is [0.5−2] keV, the exposure time 10 ks, and the three XMM instruments are added together (MOS1, MOS2 and pn). Point-like sources follow the observed $\log N - \log S$ relation and the extended sources (clearly visible on the wavelet filtered image) are clusters of galaxies with $T_{\rm X} = 3$ keV at $z = 1$ (see text for details).

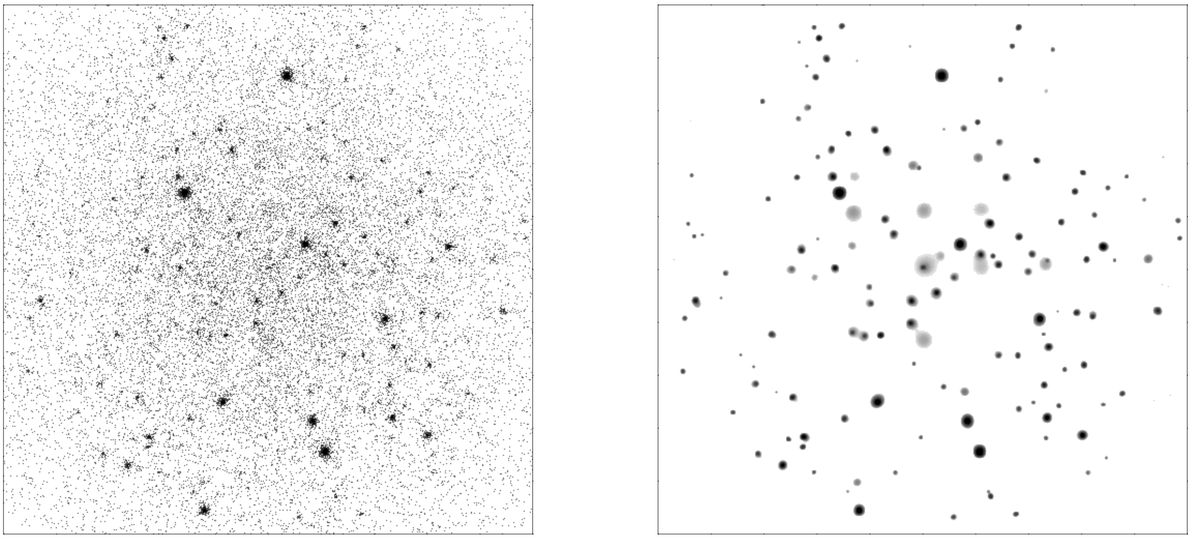

Fig. 2. Same as Fig. 1 but with clusters at $z = 1.5$.

right-hand panel of Fig. 1. The detection was performed in the same way as in VPG, i.e. using multi-scale (wavelet) filtering assuming Poisson noise statistics (Starck & Pierre 1998), followed by `SExtractor` (Bertin & Arnouts 1996) detection and classification. As was pointed out in VPG, this is currently the most suitable method to detect, characterize and classify extended sources in XMM images. The raw photon and wavelet filtered images for clusters with $T = 3$ keV at a redshifts of $z = 1$ and 1.5 are shown in Figs. 1 and 2.

To cross-identify the detected objects with the input clusters we have used a searching radius of $12''$. If a correspondence is found, we perform a classification based on the half-light radius and the stellarity index, to determine whether the object is extended. (For the choice of the searching radius and the classification criteria, see VPG). A cluster is finally considered to be detected if the positional *and* the classification criteria are obeyed. This procedure is close to the planned analysis of the incoming XMM data, which will make use of the multi-color optical data to confirm the existence of the X-ray cluster candidates.

3.2. Selection function

The selection function is a convenient way of quantifying the detection sensitivity of a survey. It was computed for a number of existing and future cluster surveys (e.g. Romer et al. 2001 for the XMM serendipitous Cluster Survey; Henry et al. 2001 for the NEP ROSAT survey; Adami et al. 2000 for the SHARC survey) using both analytical estimates and image simulations.

Here, we estimate the selection function of the XMM-LSS, by performing a set of 10 simulations for a set of temperatures ($T = 3, 4, 5, 6, 7, 8, 9$ keV) and redshifts

($z = 0.6, 1.0, 1.5, 1.8, 2.0$). For each value of T and z, the selection $\phi(T, z)$ of clusters for the survey was then calculated by comparing the number of detections (and correct classifications) $N_{\rm det}(T, z)$ to the number of input clusters $N_{\rm in}(T, z)$, so that

$$\phi(T, z) = N_{\rm det}(T, z)/N_{\rm in}(T, z). \quad (2)$$

Figure 3 shows the resulting selection function, which gives the probability for a cluster with temperature T and redshift z to be detected and classified as an extended object in the survey catalogue. Approximately, 90% of all clusters with $T > 3$ keV are detectable out to $z \sim 0.6$. The selection function is close to about 1 for $T > 2$ keV and $z < 0.5$ (not shown). Since we are only interested in clusters (and groups), we set the selection function to 0 for $T < 2$ keV at all redshifts. This corresponds to a minimum bolometric luminosity of about $1.2 \times 10^{43}\, h^{-2}$ erg s^{-1} (see Eq. (1)) and can thus be easily implemented in practice. As can be seen in the figure, low temperature clusters become progressively harder to detect as the redshift increases (compare Figs. 1 and 2). For example, at $z = 2$ only clusters with $T > 6$ keV yield a completeness better than 90%.

Our results are consistent with that of Romer et al. (2001; Fig. 5) who found that essentially all clusters with with $T > 2$ keV ($T > 4$ keV) and $z \lesssim 0.6$ ($z \lesssim 1.0$) can be detected in a survey with a sensitivity comparable to that of XMM-LSS. Note that our selection function corresponds to the average sensitivity over the inner 13 arcmin of a single XMM-EPIC pointing. The effects of sensitivity variations produced by vignetting and overlapping pointings are discussed in Sect. 6.

It is instructive to compare our selection function to that corresponding to a constant flux limit, as assumed in many previous studies. The flux $S_{[0.5-2]}$ of a cluster in the [0.5−2] keV band at redshift z can be derived from its temperature using the $L - T$ relation (Eq. (1)), the Raymond-Smith spectrum and the luminosity-distance relation. Using this correspondence, we can express the selection function in terms of the flux rather than temperature. The resulting selection function $\phi(S_{[0.5-2]}, z)$ is shown in Fig. 4. Our selection function clearly does not exactly correspond to a sharp flux limit, but is instead a smooth function of the flux. For latter comparison, we note that a detection probability of 50% corresponds approximately to a flux limit of $S_{[0.5-2]} = 10^{-14}$ erg s^{-1} cm^{-2} at the redshifts of interest.

In the following, we will use our selection function which includes most of the relevant instrumental and observational limitations. For comparison, we will also consider the selection function corresponding to the above flux limit, along with that corresponding to temperature limit $T > 2$ keV. The latter selection is useful to study the effect of the removal of small clusters on our predictions.

4. Cluster counts

We first compute the expected cluster number counts in the survey. This is done using the cluster selection function derived in the previous section combined with the Press-Schechter formalism. We first briefly review the main assumptions involved in our calculation of the mass function and of the temperature function of clusters. We then compute the expected projected number of clusters on the sky, as function of redshift. Finally, we show how the resulting redshift distribution constrains cosmological parameters within CDM models.

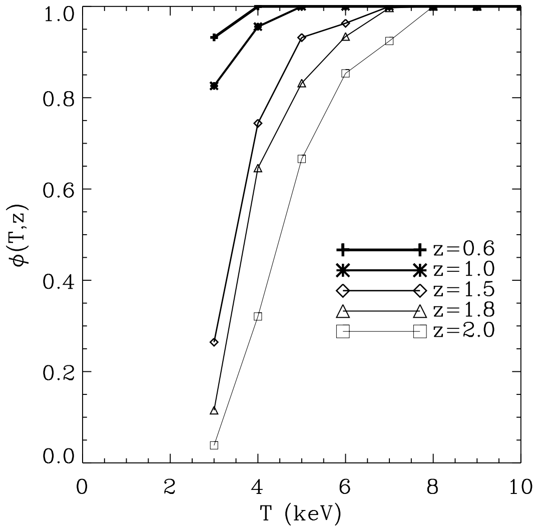

Fig. 3. Selection function $\phi(T, z)$ for ΛCDM model derived from the simulations. This function is the probability that a cluster with temperature T and redshift z is detected and classified as an extended object in the survey catalogue.

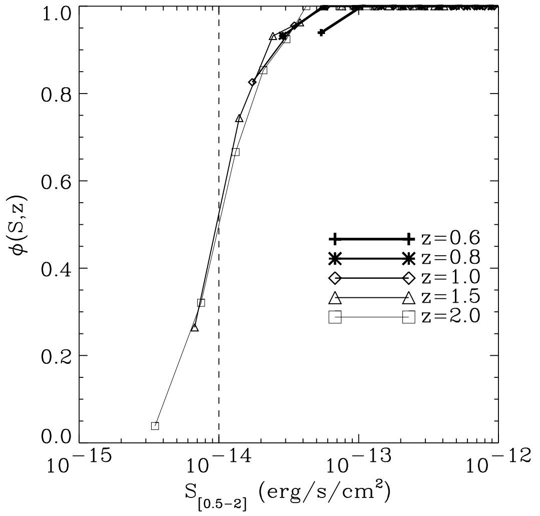

Fig. 4. Selection function $\phi(S, z)$ expressed in terms of the flux S in the [0.5−2] keV band for the ΛCDM model. Only fluxes corresponding to temperatures above our 2 keV limit are displayed. The vertical line shows a flux limit of 10^{-14} erg s^{-1} cm^{-2}; it illustrates deviations from a strict flux limit when realistic observing conditions are taken into account (esp. source confusion).

4.1. Mass function

The Press-Schechter formalism provides an analytic expression for the abundance of dark matter halos (Press & Schechter 1974). At a given redshift z, the differential number of dark matter halos of mass M per unit comoving volume is

$$\frac{{\rm d}n}{{\rm d}M} = \sqrt{\frac{2}{\pi}}\frac{\bar{\rho}}{M}\frac{{\rm d}\nu}{{\rm d}M}{\rm e}^{-\frac{\nu^2}{2}} \quad (3)$$

Table 1. Cosmological models.

Model	h	$\Omega_{\rm m}$	Ω_Λ	σ_8	Γ
τCDM	0.5	1	0	0.52	0.23
ΛCDM	0.7	0.3	0.7	0.93	0.23
OCDM	0.7	0.3	0	0.87	0.23

where $\overline{\rho}$ is the present mean matter density. The peak height is defined as $\nu(M) = \delta_{\rm c}/\sigma(M)$, where $\sigma(M)$ is the linear rms fluctuation in a sphere containing a mean mass M. We compute $\sigma(M)$ for an arbitrary cosmological model by integrating the linear power spectrum $P_{\rm lin}(k)$ derived from the BBKS transfer function (Bardeen et al. 1986; with the conventions of Peacock 1997), evolved with the linear growth factor $D(z)$. The density threshold $\delta_{\rm c}$ depends weakly on cosmology (i.e. on $\Omega_{\rm m}$ and Ω_Λ) and was computed using the fitting formulae of Kitiyama & Suto (1996).

4.2. Temperature function

The X-ray temperature of a cluster at redshift z is taken to be the virial temperature which is given by (see e.g. Eke et al. 1996)

$$kT \simeq \frac{7.75}{\beta_{\rm v}}(1+z)\Omega_{\rm m}^{\frac{1}{3}}\left(\frac{M}{M_{15}}\right)^{\frac{2}{3}}\left(\frac{\mu}{0.59}\right)\left(\frac{\Delta_{\rm c}}{178}\right)^{\frac{1}{3}}\ {\rm keV}, \tag{4}$$

where the average virial overdensity $\Delta_{\rm c}(z, \Omega_{\rm m}, \Omega_\Lambda)$ can be evaluated using the fitting formulae of Kitiyama & Suto (1996), $M_{15} = 10^{15}\ h^{-1} M_\odot$ and the value $\mu = 0.59$ for the number of particles per proton mass corresponds to a hydrogen mass fraction of 76%. The factor $\beta_{\rm v}$ is equal to about 1 for a truncated singular isothermal sphere. We adopt this value as it provides a good fit to numerical simulations (Eke et al. 1996; Bryan & Norman 1997).

Combining Eqs. (3) and (4) we can derive the differential temperature function

$$\frac{{\rm d}n}{{\rm d}T} = \frac{{\rm d}n}{{\rm d}M}\frac{{\rm d}M}{{\rm d}T}. \tag{5}$$

It is often more convenient to consider the number density of clusters with temperatures above a given minimum, $n(>T) = \int_T^\infty {\rm d}T'\ \frac{{\rm d}n(T')}{{\rm d}T}$.

To illustrate the dependence of our prediction on cosmological parameters, we consider the three cosmological models listed in Table 1, i.e a tilted (τ) CDM, ΛCDM and OCDM. The normalization of these models is determined by σ_8, the amplitude of mass fluctuations on 8 h^{-1} Mpc scale. Our chosen numerical values correspond to the constraints derived from current cluster surveys, namely $\sigma_8 \simeq 0.52\Omega_{\rm m}^{-0.52+0.13\Omega_{\rm m}}$ for the flat case and $\sigma_8 \simeq 0.52\Omega_{\rm m}^{-0.46+0.10\Omega_{\rm m}}$ for the open case (Eke et al. 1996). The shape of the matter power spectrum is controlled by the shape parameter Γ which, unless otherwise specified, we fix at 0.23, as indicated by galaxy clustering surveys (see Viana & Liddle 1996 and reference therein).

4.3. Projected cluster counts

From the temperature function $\frac{{\rm d}n}{{\rm d}T}$ (Eq. (5)), we can compute the projected surface density of clusters on the sky. Noting that the comoving volume element is ${\rm d}V = R^2{\rm d}\chi{\rm d}\Omega$, where ${\rm d}\Omega$ is the infinitesimal solid angle, χ is the comoving radius and $R(\chi)$ is the comoving angular-diameter radius, we find that the number of clusters per unit solid angle, temperature and redshift interval is

$$\frac{{\rm d}N}{{\rm d}T{\rm d}z} = R^2\frac{{\rm d}\chi}{{\rm d}z}\frac{{\rm d}n}{{\rm d}T}, \tag{6}$$

where $\frac{{\rm d}\chi}{{\rm d}z} = -\frac{c}{H_0}\left[(1-\Omega)a^{-2} + \Omega_{\rm m}a^{-3} + \Omega_\Lambda\right]^{-\frac{1}{2}}$ as derived from the Friedmann equations. As a result the observed surface density of clusters per unit redshift

$$\frac{{\rm d}N_{\rm obs}}{{\rm d}z} = \int {\rm d}T\frac{{\rm d}N}{{\rm d}T{\rm d}z}\phi(T,z) \tag{7}$$

where $\phi(T,z)$ is the survey selection function (Eq. (2)).

4.4. Predictions

The predicted projected counts as a function of redshift are shown in Fig. 5 for the three cosmological models whose parameters are listed in Table 1. The counts correspond to the full 64 deg^2 of the completed XMM-LSS survey. The counts from the three models agree at low redshifts ($z < 0.2$), as expected since the three models were normalized with the number of clusters in the local universe. On the other hand, the number counts differ greatly at larger redshifts. The τCDM model predicts much smaller number of clusters at $z > 0.2$, while the ΛCDM and OCDM models differ for $z > 0.6$. The predicted counts at $z > 1$ are larger in the OCDM model compared to that in the ΛCDM case, due to the somewhat slower evolution of the growth factor in the open model. These differences illustrate the well known fact that the evolution of cluster counts is a powerful probe of $\Omega_{\rm m}$ and Ω_Λ. Note that our predictions implicitly rely on the $L-T$ relation of Eq. (1), which was used to derive the selection function $\phi(T,z)$ from the simulations (see Sect. 3).

In the 64 deg^2 of the survey, the expected number of detected clusters with $0 < z < 1$ (and $T > 2$ keV) is about 900, 1000 and 175 for the ΛCDM , OCDM and τCDM model, respectively. For $1 < z < 2$, the expected counts are about 400, 900 and <10, for each model respectively. Our total number of clusters for $0 < z < 2$ of about 1300 in the former model, is in approximate agreement with the predictions of Moscardini et al. (2000) who predict about 1100 clusters in the XMM-LSS for a ΛCDM model with slightly different flux and temperature thresholds.

Figure 7 shows how these predictions for the ΛCDM model depend on σ_8 and $\Omega_{\rm m}$. Clearly, the number counts are very sensitive on these two parameters. Taking $\sigma_8 = 0.93 \pm 0.07$ for $\Omega_{\rm m} = 0.3$ (Eke et al. 1996), the expected number of clusters in this model is between 600–1200 for $0 < z < 1$ and 200–700 for $1 < z < 2$.

The effect of the selection function on these predictions are shown in Fig. 6. The number counts for the ΛCDM model

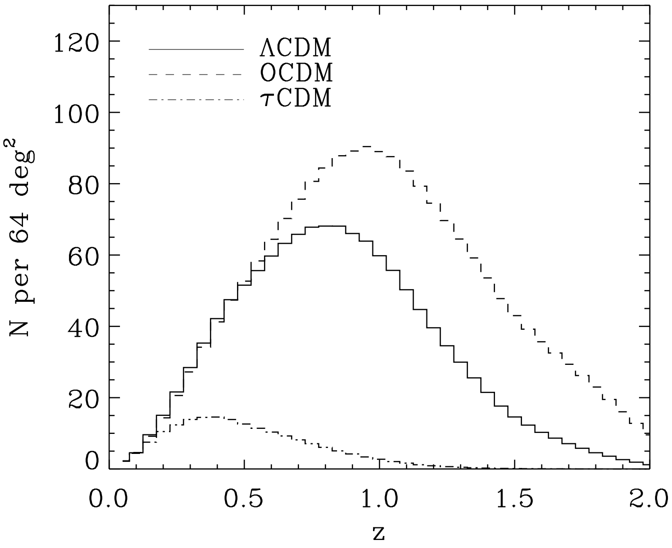

Fig. 5. Projected number counts of clusters as a function of redshift in the three cosmological models. The selection function $\phi(T, z)$ for the XMM-LSS derived from image simulations was used for each model. The redshift bins have a width of $\Delta z = 0.05$.

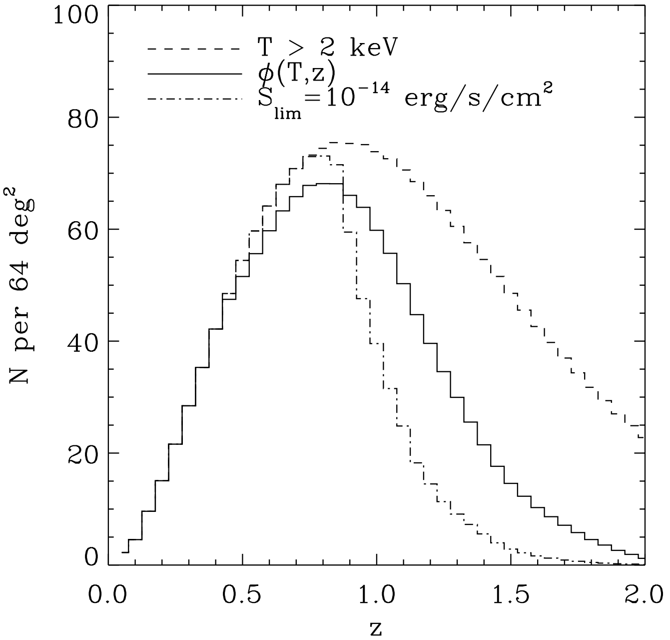

Fig. 6. Projected number counts of clusters for the ΛCDM model with different selection criteria: with the selection function $\phi(T, z)$ (as in Fig. 5), with a temperature limit only ($kT > 2$ keV), and with a flux limit ($S_{[0.5-2]} > 10^{-14}$ erg s^{-1} cm^{-2}). Again, the redshift bins have a width of $\Delta z = 0.05$.

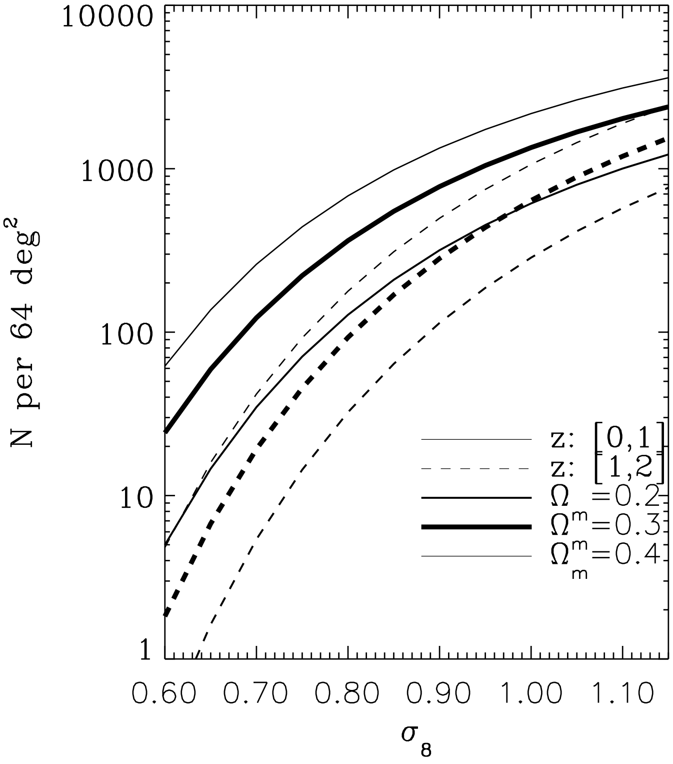

Fig. 7. Cluster counts expected for the XMM-LSS as a function of σ_8 and $\Omega_{\rm m}$ in the ΛCDM model. The XMM-LSS simulated selection function was used in all cases. Counts for the $0 < z < 1$ and $1 < z < 2$ redshift intervals are shown as the solid and dashed lines, respectively. In each case, models with $\Omega_{\rm m} = 0.4$, 0.3 and 0.2, are shown from top to bottom, respectively.

are shown as a function of redshift, for our selection function $\phi(T, z)$ (as in Fig. 5), for the flux limited case and for the temperature limited case. For $z \gtrsim 0.9$, the counts with the selection function are larger than the flux limited counts. This is expected, since a large number of clusters fainter than the flux limit contribute to the $\phi(T, z)$ counts because of the tail of the selection function (see Fig. 4). This demonstrates the importance of considering all the observational details when making such predictions, especially confusion by point-like sources, an unavoidable drawback for a highly sensitive instrument. Notice that the temperature limited counts agree with the other two for $z < 0.4$. This shows that our counts are limited mainly by the temperature at low redshifts. Not surprisingly, the T-limited counts overpredict the abundances for $z > 0.4$. As a check, we have compared our predictions with that of Romer et al. (2001). For their effective flux limit of $S_{[0.5-2]} > 1.5 \times 10^{-14}$ erg s^{-1} cm^{-2} and $kT > 2$ keV, we find that our predictions agree very well with the counts shown in their Fig. 6c.

Note that the fluxes of the clusters measured in XMM-LSS will be rather uncertain (see VPG). This will prevent us from making accurate determinations of the luminosity, and therefore of the temperature and of the mass, of each cluster. In this paper, we therefore consider statistical quantities (such as the counts and the correlation function) which are averaged over the population of clusters detectable in the survey, and therefore do not require this information. A study of the further constraints which can be derived from the (uncertain) flux measurements is left to future work.

4.5. Cosmological constraints from cluster counts

We now wish to study how the cluster counts can be used to constrain cosmological parameters. For this purpose, we generated cluster counts from the predicted counts from Eq. (7) in

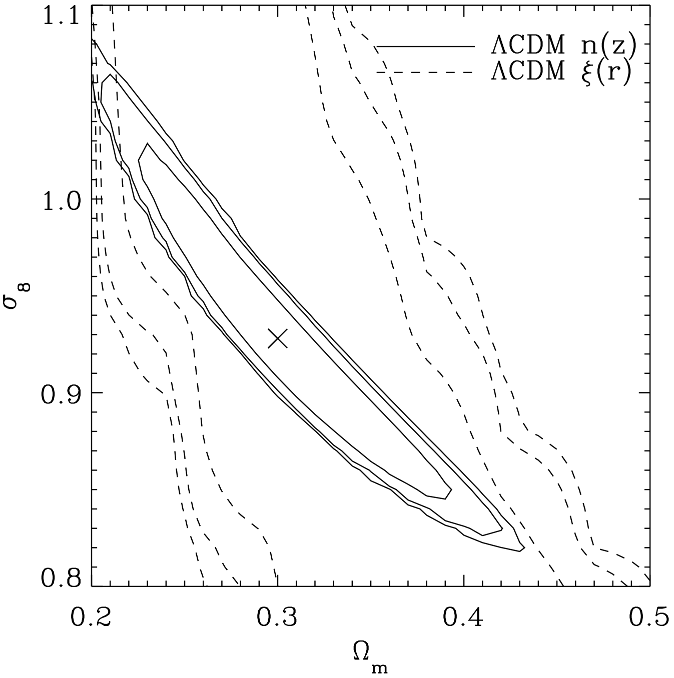

Fig. 8. Constraints on the cosmological parameters Ω_m and σ_8 for the ΛCDM model, from the cluster counts (solid lines) and from the correlation function (dashed lines). In each case, the 68%, 90% and 95% confidence level contours are shown along with the assumed model (cross).

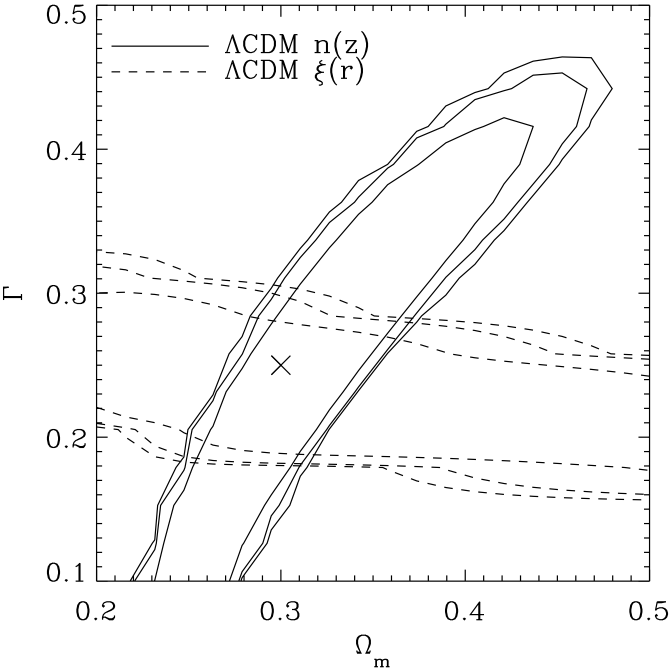

Fig. 9. Constraints on Γ and Ω_m for the ΛCDM model, from the cluster counts (solid lines) and from the correlation function (dashed lines). As before, the 68%, 90% and 95% confidence level contours are shown (solid lines) along with the assumed model (cross).

ΛCDM model for several redshift bins (as shown in Fig. 5 for different models). We used the XLSS selection function $\phi(T, z)$ and survey area, and considered redshift bins of width $\Delta z = 0.1$ from $z = 0$ to $z = 1$ assuming Poissonian errors for the number counts in each bin. Note that the Poisson errors neglect the uncertainty arising from cosmic variance; this is a good approximation since this latter uncertainty is small for a survey area as large as that of the XLSS (compare the correlation length ~20 h^{-1} Mpc to the survey size, ~200 h^{-1} Mpc at $z \simeq 0.5$). We then calculated the χ^2-difference between the simulated counts and that expected in a ΛCDM model for a range of values for σ_8 and Ω_m. This approach is rather computer intensive, but it is more accurate than the faster Fisher matrix method, which approximates the confidence regions as ellipses and can be incorrect when the parameter space is non-Gaussian (Holder et al. 2001). Note that our χ^2 fitting method is only strictly valid for gaussian errors. This is however a good approximation in our case, given the large number of clusters in the redshift bins shown in Fig. 5, further enhanced by our use of $\Delta z = 0.1$ bins rather than 0.05 in the figure.

The resulting constraints on these cosmological parameters are shown as the solid lines in Fig. 8. The input ΛCDM model is that of Table 1 and is shown with a cross. The 90% and 95% confidence regions are shown as solid lines. The cluster counts alone will provide tight constraints on both parameters, with 95% uncertainties of about 0.06 and 0.05 for σ_8 and Ω_m, respectively. As can be seen from the elongation of the contours, the two parameters are however somewhat degenerate. Any additional information on either parameters, can thus be used to reduce their respective uncertainty. Note that these constraints only reflect statistical errors, and neglect potentially important systematic uncertainties in the scaling laws of clusters. A discussion of the limitations imposed by systematics on our predictions is presented in Sect. 6.

It is also interesting to investigate how cluster counts can constrain Γ, the shape parameter of the matter power spectrum. For this purpose, we follow the same χ^2 procedure, this time varying Γ and Ω_m, while σ_8 follows the Eke et al. (1996) relation (see Sect. 4.2). The resulting confidence contours for the ΛCDM model are shown as the solid lines in Fig. 9. Clearly, these two parameters are quite degenerate with counts alone, hampering the determination of Ω_m, which can only be determined with an accuracy of about 40% (95% CL). More information is therefore required to alleviate these limitations. One obvious possibility is to use other measures of large-scale structure such as galaxy catalogues to constrain Γ. This has the disadvantage of relying on assumptions about the bias of galaxies and on an external data set. In the next section, we show how the degeneracy can be broken by measuring the correlation function of the galaxy cluster population.

5. Cluster correlation function

We now turn to the cluster correlation function which quantifies the spatial clustering of clusters in the survey. We first use the extended halo model of Mo & White (1996) to predict the observed cluster correlation function at a given redshift. We then consider the average correlation function in a finite redshift range, compute its uncertainties, and study the constraints its measurement can place on cosmological parameters.

5.1. Observed correlation function: At a single redshift

According to the Mo & White (1996) halo formalism, the correlation function of two sets of clusters with masses M and M' and with comoving separation r is given by

$$\xi(r, M, M', z) \simeq b(M, z) b(M', z) \xi_{\rm lin}(r, z), \tag{8}$$

where $\xi_{\rm lin}(r, z) = \xi_{\rm lin}(r, 0) D^2(z)$ is the linear correlation function which is the Fourier Transform of the linear power spectrum $P_{\rm lin}(k, z)$. The mass dependent bias parameter of the halos is given $b(M, z) = 1 + (\nu^2 - 1)/\delta_{\rm c}$, with the conventions of Sect. 4.1. Note that the separation of the clusters is assumed to be small compared to the scale in which any evolution takes place.

It is easy to show that the resulting observed correlation function in a narrow redshift interval is given by (Suto et al. 2000; Moscardini et al. 2000 and reference therein)

$$\xi_{\rm obs}(r, z) = b_{\rm eff}^2(z) \xi_{\rm lin}(r, z), \tag{9}$$

where the effective bias is

$$b_{\rm eff}(z) = \int {\rm d}M \frac{{\rm d}n_{\rm obs}}{{\rm d}M} b(M) \Bigg/ \int {\rm d}M \frac{{\rm d}n_{\rm obs}}{{\rm d}M}\ , \tag{10}$$

and where the observed differential number counts are given by $\frac{{\rm d}n_{\rm obs}}{{\rm d}M} = \frac{{\rm d}n}{{\rm d}T} \frac{{\rm d}T}{{\rm d}M} \phi(T, z)$. Note that, in our analysis, we neglect redshift-space distortions which were shown to yield only about 10% corrections on the amplitude of the correlation function (Suto et al. 2000; Moscardini et al. 2000).

In general, the evolution of $\xi_{\rm obs}(r, z)$ is determined by two competing effects. First, the growth of structures induces the linear correlation function $\xi_{\rm lin}(r, z)$ to decrease as the redshift increases. On the other hand, the clusters which are detectable at large redshifts are more massive and therefore more strongly biased. The effective bias $b_{\rm eff}(z)$ thus tends to be larger at high redshift. To study the interplay between these two effects it is convenient to define

$$b_{\rm eff,0}(z) \equiv \left[\frac{\xi_{\rm obs}(r, z)}{\xi_{\rm lin}(r, 0)} \right]^{\frac{1}{2}} = b_{\rm eff}(z) D(z). \tag{11}$$

This quantity provides the bias of the observed cluster correlation with respect to the linear correlation function at $z = 0$, and therefore quantifies the evolution of the correlation function.

The behaviour of $b_{\rm eff,0}(z)$ is shown in Fig. 10 for the three cosmological models and for the XMM-LSS selection function. The curves are remarkably flat for all models, showing that the cluster correlation function evolves only very weakly from $z = 0$ to $z = 2$. It is interesting to study whether this lack of evolution depends on the selection function. Figure 11 shows $b_{\rm eff,0}(z)$ for each selection scheme for the ΛCDM model. The evolution is also very weak for the temperature limited case. For the flux-limited sample, the evolution is stronger for $z > 1$. This evolution is lost when the full selection function $\phi(T, z)$ is used. In all cases, there is effectively no evolution for $0 < z < 1$. We shall thus, in the following, derive the constraints on cosmology integrating the correlation function over the $0 < z < 1$ range.

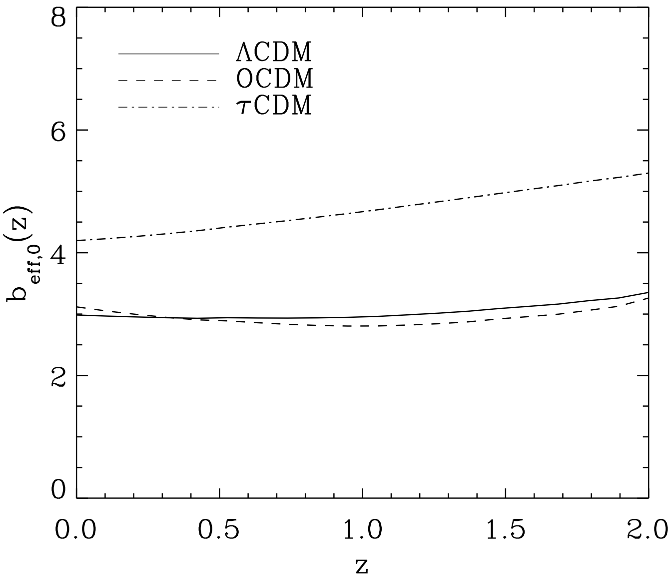

Fig. 10. Evolution of $b_{\rm eff,0}(z)$, the effective bias of the cluster correlation function $\xi_{\rm obs}(r, z)$ with respect to the linear mass correlation function $\xi_{\rm lin}(r, 0)$ at $z = 0$. This quantifies the evolution of the cluster correlation function. It is shown for the three cosmological models as a function of redshift.

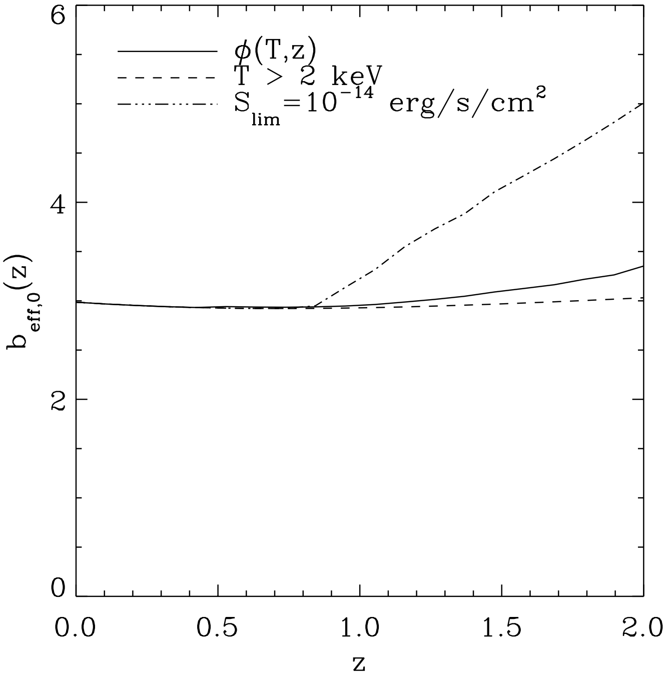

Fig. 11. Evolution of $b_{\rm eff,0}(z)$ in the ΛCDM model for different selection schemes: the XMM-LSS selection function, a temperature limited survey, and a flux limited survey.

5.2. Observed correlation function: Redshift average

To maximize the sensitivity, it is useful to measure the correlation function over a wide redshift range. In this case, we must take into account the pair-weighted evolution of the correlation function $\overline{\xi}(r, z)$ within the light-cone section of interest. The average correlation function in the redshift interval

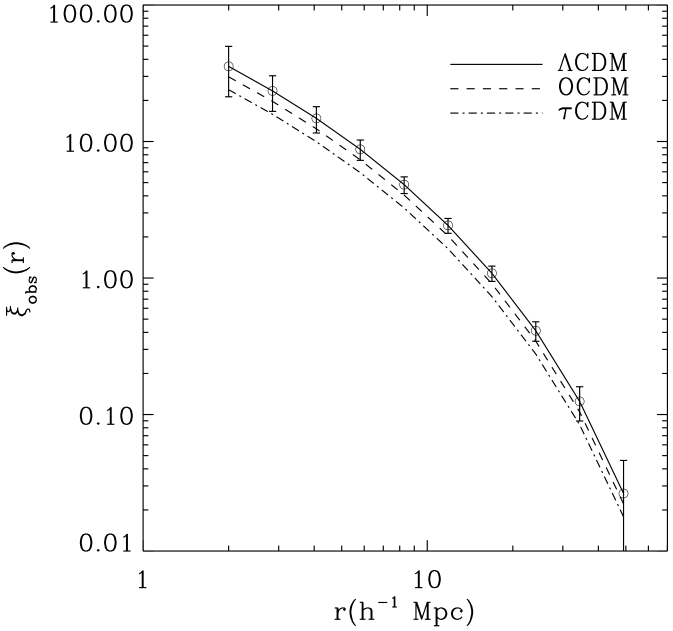

Fig. 12. Prediction for the cluster correlation function averaged in redshift interval $0 < z < 1$. The three cosmological models are shown. For clarity, the expected measurement error bars for the full 64 deg^2 of the XMM-LSS are shown only for the ΛCDM model.

$z_{\rm min} < z < z_{\rm max}$ is thus given by (Suto et al. 2000; Moscardini et al. 2000 and reference therein)

$$\bar{\xi}_{\rm obs}(r) = \frac{\int_{z_{\rm min}}^{z_{\rm max}} {\rm d}z\, \frac{{\rm d}\chi}{{\rm d}z} R^2 n_{\rm obs}^2(z) \xi_{\rm obs}(r,z)}{\int_{z_{\rm min}}^{z_{\rm max}} {\rm d}z\, \frac{{\rm d}\chi}{{\rm d}z} R^2 n_{\rm obs}^2(z)}, \tag{12}$$

where the observed number density of clusters is $n_{\rm obs}(z) = \int {\rm d}T \frac{{\rm d}n}{{\rm d}T} \phi(T,z)$.

The resulting correlation functions for the three cosmological models are shown in Fig. 12. The XMM-LSS selection function was used in all cases, along with a redshift range of $0 < z < 1$. The correlation functions for the 3 models have very similar shape, as expected since the same value for Γ was assumed in all cases. Notice that the τCDM correlation function has a lower amplitude than that for the other two models. This is expected since the former model has a lower value for σ_8 (see Table 1). The ΛCDM and OCDM models have very similar values of σ_8 and thus yield correlation functions with very similar amplitudes.

Our predictions are in good agreement with the results of Moscardini et al. (2000). In particular, for our ΛCDM model, these authors find a correlation length r_0 (defined by $\bar{\xi}_{\rm obs}(r_0) \equiv 1$) of about 13 and 15 h^{-1} Mpc for $z < 0.3$ and $z > 0.3$, respectively. This is to be compared with our value of $r_0 \simeq 17\ h^{-1}$ Mpc for $z < 1$. We also verified that the evolution of the correlation function is weak if we adopt their assumed strict flux limit of $S_{[0.5-2]} = 5 \times 10^{-15}$ erg s^{-1} cm^{-2}.

5.3. Uncertainties

We now wish to estimate the uncertainty involved in measuring the cluster correlation function. The simplest way to measure the correlation function is to count the number of pairs in excess of random in the survey volume. (This is sometimes taken as the definition of the correlation function.) An estimator for $\bar{\xi}_{\rm obs}(r)$ in a bin of radii between r and $r + \Delta r$ is thus

$$\hat{\bar{\xi}}_{\rm obs}(r, \Delta r) \equiv \frac{N_{\rm pairs}^{\rm obs}(r, \Delta r)}{N_{\rm pairs}^{\rm ran}(r, \Delta r)} - 1, \tag{13}$$

where $N_{\rm pairs}^{\rm obs}$ and $N_{\rm pairs}^{\rm ran}$ are the number of pairs (i.e. with clustering) and for a random distribution (i.e. without clustering), respectively, in the observed radius interval. Ignoring boundary effects, the random number of pairs is given by

$$N_{\rm pairs}^{\rm ran}(r, \Delta r) \simeq 2\pi A r^2 \Delta r \int_{z_{\rm min}}^{z_{\rm max}} {\rm d}z \frac{{\rm d}\chi}{{\rm d}z} R^2 n_{\rm obs}^2(z), \tag{14}$$

where A is the solid angle of the survey.

For weak signals, the error in measuring $\hat{\bar{\xi}}_{\rm obs}(r, \Delta r)$ will be dominated by Poisson statistics, and will thus be given by (see e.g. Peebles 1980)

$$\sigma[\hat{\bar{\xi}}_{\rm obs}(r, \Delta r)] \simeq \frac{1 + \xi(r)}{\sqrt{N_{\rm pairs}^{\rm obs}(r, \Delta r)}} = \sqrt{\frac{1 + \xi(r)}{N_{\rm pairs}^{\rm ran}(r, \Delta r)}}. \tag{15}$$

This provides us with an expression for the error in the correlation function for a finite survey. The resulting errors for the ΛCDM model and for the full 64 deg^2 of the XMM-LSS are shown in Fig. 12. Again, these errors only reflect statistical errors and neglect uncertainties in the cluster scaling relations. A discussion of the impact of systematics, including that arising from spatial variations of the survey sensitivity, is presented in Sect. 6.

5.4. Combined cosmological constraints

We now study how the measurement of the cluster correlation function constrains cosmological parameters. As for the cluster counts (Sect. 5.4), we use a χ^2-fit to simulated measurements of the correlation function to derive confidence regions in parameter space. We considered a redshift interval of $0 < z < 1$ and computed the errors using Eq. (15).

The resulting confidence contours for a joint fit of $\Omega_{\rm m}$ and σ_8 are shown as the dashed lines in Fig. 8, for the ΛCDM model. The constraints from the correlation function are rather weak on this plane alone, with little dependence on σ_8. These constraints are however somewhat orthogonal to that from cluster counts and are thus complementary.

The constraints from the correlation function on Γ and $\Omega_{\rm m}$ are shown in Fig. 9. The shape of the resulting confidence contours agrees qualitatively with the predictions of Moscardini et al. (2000) for the shallower REFLEX survey. The contours show little dependence on $\Omega_{\rm m}$ and are therefore nearly orthogonal to that from cluster counts alone. With the combined counts and correlation function constraints, $\Omega_{\rm m}$, σ_8 and Γ can be measured with a precision of about 15%, 10%, and 35%, respectively at the 95% confidence level. The cluster correlation function thus provides the required information to break the degeneracy present when cluster counts alone are considered.

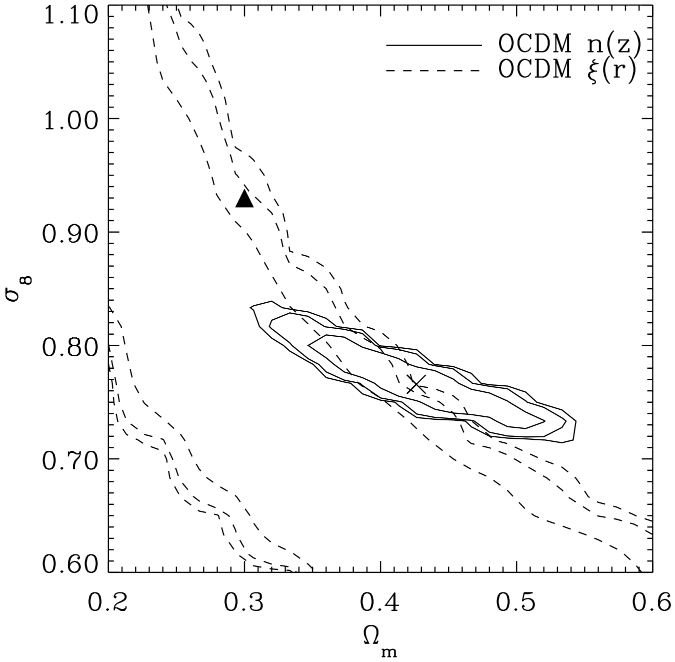

Fig. 13. Constraints on $\Omega_{\rm m}$ and σ_8 resulting from a fit of the OCDM model to the ΛCDM predictions. Both the cluster counts (solid lines) and the correlation function (dashed lines) are shown. In each case, the 68%, 90% and 95% confidence level contours are shown, along with the χ^2 minimum (cross) and the input values for the ΛCDM model (filled triangle).

The impact of systematics on these constraints is discussed in Sect. 6.

Until now, we have focused on the ΛCDM model, thus implicitely assuming prior knowledge that the universe is flat. While flatness is strongly indicated by measurements of the Cosmic Microwave Background anisotropies (e.g. Jaffe et al. 2001), it is interesting to establish whether our predictions depend on this assumption. To study this, we fitted an OCDM model to the ΛCDM predictions for both the cluster counts and the correlation function. The resulting constraints on σ_8 and $\Omega_{\rm m}$ are shown in Fig. 13. For the cluster counts, the best fit values for both of these parameters are now biased (compare the best fit, cross, to the input values, triangle). This bias again hampers the determination of $\Omega_{\rm m}$ using cluster counts alone. Thankfully, the correlation function can again help overcome this limitation. Indeed, the contours for $\xi(r)$ are now somewhat incompatible with that from the counts (compare to Fig. 8). The consistency between the counts and correlation function constraints can thus be used as a diagnostic and as a discriminant between the ΛCDM and the OCDM model.

6. Systematic uncertainties

So far in our analysis, we have neglected systematic uncertainties. Here we review the major source of systematics and discuss their impact on our predictions[4].

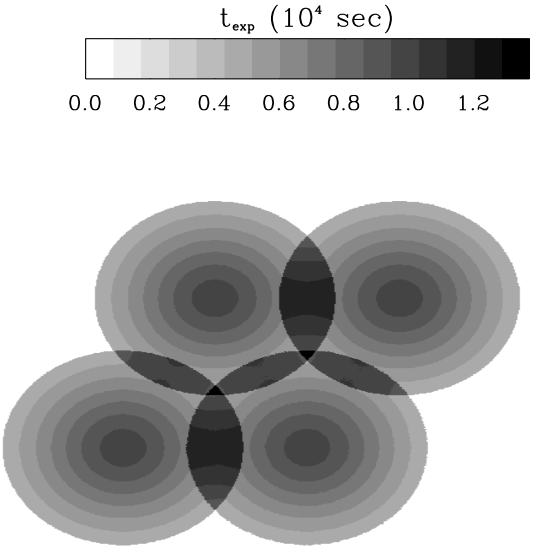

Fig. 14. Exposure time map for the XMM-LSS tiling pattern. Four XMM fields are displayed out to a maximum radius of 13′. The fields are separated by 20 arcmin from each other.

First, we have assumed that the $L-T$ and $M-T$ relations were perfectly known. Physical processes such as feedback from star formation and reionization, can modify these relationships and therefore yield detectable changes in the cluster counts and correlation function (see e.g. Muanwong et al. 2001 and reference therein). These could perhaps explain the discrepancy which has recently been found between the observed $M-T$ relation and that derived from numerical simulations (see Finoguenov et al. 2001; Allen et al. 2001 and reference therein). Cluster mergers have also been shown to produce sharp temperature and luminosity jumps, thus likely affecting the $L-T$ relation (Ricker & Sarazin 2001). Another important issue is the existence of high redshift cooling flows which may affect the detectability of distant clusters and their $L-T$ relation (e.g. Henry 2000).

By the time the XMM-LSS is completed, better insights will be gained about these various physical effects, thanks to deep pointed observations of clusters with XMM and Chandra. An interesting way of parameterizing the residual uncertainties has been proposed by Diego et al. (2001). These authors kept the normalisation and evolution of the different cluster scaling relations as free parameters, and studied the resulting degeneracies with cosmological parameters. It would be interesting to extend their approach to include constraints from the cluster correlation function. The study of these pending theoretical questions is left for future work.

In our simulation, we have also assumed that the core radius $r_{\rm c}$ is fixed. More realistically, the core radius could vary with mass and redshift. For instance, Jones et al. (1999) found a correlation between core radii and temperatures in a cluster sample from the *Einstein* mission. Our detection sensitivity depends most strongly on the cluster flux, which is independent of the core radius in our simulations. A varying $r_{\rm c}$ is therefore unlikely to affect our selection function very much, except perhaps in our ability to separate clusters from point sources.

---

[4] We thank Kathy Romer, the referee, for her many suggestions which are included in this section.

Another systematic effect arises from our assumption of a sharp temperature cutoff ($kT > 2$ keV) for our cluster selection. Since temperatures will not be available with XMM-LSS, this will be enforced in practice by setting a luminosity cutoff, derived from the observed fluxes and redshifts. Because the luminosity function is very steep, the errors in the observed fluxes will lead to a bias tending to include low mass clusters in the counts. This effect can be corrected for by running simulations similar to ours, but which would include objects with $kT < 2$ keV.

Another complication is induced by variations in the detection sensitivity over the survey area. Figure 14 shows the effective exposure time for the XMM-LSS tiling strategy, in which the 10 ksec exposures are separated by 20 arcmin. As is apparent in the figure, vignetting causes variations in the exposure time of about 50%, corresponding to flux sensitivity variations of about 25%. This will affect both the uniformity of the cluster counts and the observed cluster correlation function. Since the vignetting function is well calibrated, the sensitivity variations can however be accurately predicted and corrected for. This can be done by using further image simulations to compute the selection function as a function of position. Note that, in the simulations we have presented in Sect. 3, we have only computed the average selection function by placing clusters throughout the inner 13′ of a single XMM-EPIC pointing. Our detection limits are thus conservative, as they do not include the increased sensitivity afforded in the regions of overlap of two XMM fields.

7. Conclusions

Following the REFLEX survey (Guzzo et al. 1999; Böhringer et al. 2001) based on the ROSAT All-Sky-Survey and the NEP ROSAT survey (Henry et al. 2001), the XMM-LSS survey will be about 1000 and 10 times deeper, respectively, and thus opens wide prospects for cosmology. Indeed, it will provide an independent measurement of cosmological parameter and thus complements Cosmic Microwave Background and Supernova experiments. It will also provide a test of important ingredients of the standard cosmological model, such as the gravitational instability paradigm and the gaussianity of initial fluctuations.

To study the constraints XMM-LSS will set on cosmological parameters, we first derived the selection function for the survey using detailed simulations of cluster detection in XMM-Newton images. We found that our selection function differs significantly from a simple flux-limit selection. We then computed the expected number counts of clusters in several CDM models. We found that, for the currently favoured ΛCDM model, we expect about 600-1200 clusters to be detectable in XMM-LSS at $0 < z < 1$ and about 200–700 at $1 < z < 2$, the uncertainty being dominated by the current errors on σ_8 and $\Omega_{\rm m}$.

Clusters counts beyond $z > 0.5$ depend on cosmological parameters and can thus be used to constrain models. Within a ΛCDM model, we found that the redshift dependence of the XMM-LSS cluster counts will allow us to measure σ_8 and $\Omega_{\rm m}$ with a precision of about 6% and 18% (95% CL), respectively, if the shape parameter Γ is known. In the absence of prior knowledge on Γ, the precision on these parameters degrades considerably, if only cluster counts are considered.

This limitation can be circumvented by considering the cluster correlation function. One of the strength of XMM-LSS is indeed to offer a uniform coverage over a wide contiguous area (64 deg^2), with an extensive spectroscopic follow-up. This will allow us to measure the correlation function in several redshift bins out to $z = 1$. Using the extended halo formalism of Mo & White (1996), we computed the correlation function of clusters detectable in XMM-LSS. We find that, for the selection function of XMM-LSS, the correlation function is not expected to evolve significantly from $z = 0$ to 2. This results from the competing effects of the growth of mass perturbations and the stronger bias of the detectable massive clusters at large redshifts. It will thus be important to compare the correlation function measured in two redshift bins between $z = 0$ and $z = 1$: the verification of the lack of evolution provides a test of the bias model for haloes and of the gravitational instability paradigm.

The amplitude and shape of the cluster correlation function can be used to lift the degeneracies present when cluster counts alone are considered. Within a ΛCDM model, the correlation function function measured in XMM-LSS at $0 < z < 1$, combined with the cluster counts, will constrain $\Omega_{\rm m}$, σ_8 and Γ with a precision of about 15%, 10% and 35%, respectively (95% CL). Moreover, the combination of the counts and the correlation function will provide a consistency check for the ΛCDM model, and a discrimation between this model and the OCDM model. The XMM-LSS therefore has great potentials for the measurement of cosmological parameters. Note however that the above constraints only reflect statistical errors and ignore the limitations arising from systematic uncertainties. Instrumental systematics, such as sensitivity variations, could be important but can be accurately corrected using further image simulations. Systematic uncertainties in the cluster scaling relations may also contribute significantly to the error budget. By the time the XMM-LSS is completed, better knowledge of these scaling relations will have been derived from deeper pointed observations with XMM and Chandra. The study of the impact of potential residual uncertainties on cosmological constraints with XMM-LSS is left for future work.

Acknowledgements. We thank Kathy Romer, the referee, for her useful comments and criticisms, and for her numerous suggestions regarding systematic effects. AR was supported by a TMR postdoctoral fellowship from the EEC Lensing Network, and by a Wolfson College Research Fellowship.

References

Adami, C., Ulmer, M. P., Romer, A. K., et al. 2000, ApJS, 131, 391

Allen, S. W., Schmidt, R. W., & Fabian, A. C. 2001, MNRAS, 328, 37

Arnaud, K. A. 1996, in Astronomical Data Analysis Software and Systems V, ed G. H. Jacoby, & J. Barnes (San Francisco: ASP), ASP Conf. Ser., 101, 17 (XSPEC)

Arnaud, M., & Evrard, A. 1999, MNRAS, 305, 631

Bardeen, J. M., Bond, J. R., Kaiser, N., & Szalay, A. S. 1986, ApJ, 304, 15

Bertin, E., & Arnouts, S. 1996, A&AS, 117, 393
Borgani, S., & Guzzo, L. 2001, Nature, 409, 39
Böhringer, H., Schueker, P., Guzzo, L., et al. 2001, A&A, 369, 826
Bryan, G. L., & Norman, L. 1997, Computational Astrophysics; 12th Kingston Meeting on Theoretical Astrophysics, ASP Conf Ser., 123, 363
Cavaliere, A., & Fusco-Femiano, R. 1976, A&A, 49, 137
Collins, C. A., Guzzo, L., Böhringer, H., et al. 2000, MNRAS, 319, 939
Diego, J. M., Martínez-Gonzáles, E., Sanz, J. L., Cayón, L., & Silk, J. 2001, MNRAS, 325, 1533
Eke, V. R., Cole, S., & Frenk, C. S. 1996, MNRAS, 282, 263
Eke, V. R., Navarro, J. F., & Frenk, C. S. 1998, ApJ, 503, 569
Finoguenov, A., Reiprich, T. H., & Böhringer, H. 2001, A&A, 368, 749
Giacconi, R., Rosati, P., Tozzi, P., et al. 2001, ApJ, 551, 624
Guzzo, L., Böhringer, H., Schuecker, P., et al. 1999, ESO Messenger, 95, 27
Haiman, Z., Mohr, J. J., & Holder, G. 2001, ApJ, 553, 545
Hasinger, G., Altieri, B., Arnaud, M., et al. 2001, A&A, 365, L45
Henry, J. P. 2000, ApJ, 534, 565
Henry, J. P., et al. 2001, ApJ, 553, L109
Holder, G., Haiman, Z., & Mohr, J. J. 2001, ApJL, submitted [`astro-ph/0105396`]
Jaffe, A., et al. 2001, Phys. Rev. Lett., 86, 3475
Jones, C., & Forman, W. 1999, ApJ, 511, 65
Kitiyama, T., & Suto, Y. 1996, ApJ, 469, 480
Kitayama, T., & Suto, Y. 1997, ApJ, 490, 557
Mo, H. J., & White, S. D. M. 1996, MNRAS, 282, 347
Mo, H. J., Jing, Y. P. & White, S. D. M. 1996, MNRAS, 282, 1096
Moscardini, L., Matarrese, S., & Mo, H. J. 2000 [`astro-ph/0009006`]
Muanwong, O., Thomas, P. A., Kay, S. T., Pearce, F. R., & Couchman, H. M. P. 2001, ApJ, 552, L27
Oukbir, J., & Blanchard, A. 1997, A&A, 317, 1
Peacock, J. A. 1997, MNRAS, 284, 885
Peebles, P. J. E. 1980, The Large-Scale Structure of the Universe (Princeton: Princeton Univ. Press)
Pierre, M. 2000, Procs. of Mining the sky, Joint MPA/ESO/MPE conference, preprint [`astro-ph/0011166`]
Press, W. H., & Schechter, P. 1974, ApJ, 187, 425
Raymond, J. C., & Smith, B. W. 1977, ApJS, 35, 419
Ricker, P. M., & Sarazin, C. L. 2001, ApJ, 561, 621
Robinson, J. 2000, MNRAS, submitted [`astro-ph/0004023`]
Romer, A. K., Viana, P. T. P., Liddle, A. R., & Mann, R. G. 2001, ApJ, 547, 594
Sadat, R., Blanchard, A., & Oukbir, J. 1998, A&A, 329, 21
Starck, J.-L., & Pierre, M. 1998, A&AS, 128, 397
Suto, Y., Yamamoto, K., Kityama, T., & Jing, Y. P. 2000, ApJ, 534, 551
Valtchanov, I., Pierre, M., & Gastaud, R. 2001, A&A, 370, 689 (VPG)
Viana, P. T. P, & Liddle, A. R. 1996, MNRAS, 281, 323
Viana, P. T. P, & Liddle, A. R. 1999, MNRAS, 303, 535
Watson, M. G., Augueres, J.-L., Ballet, J., et al. 2001, A&A, 365, L51